Strong Electronic Interactions of the Abundant Cu/Ce Interfaces Stabilized Cu$_2$O for Efficient CO$_2$ Electroreduction to C$_{2+}$ Products under Large Current Density

Yuanrui Li, Jinshuo Zou, Lidan Sun, Siqi Liu, Huiqi Li, Zhongxin Song, Jun Yu,* Lei Zhang,* and Zaiping Guo*

Copper-based nanocatalysts, represented by Cu$_2$O nanocubes, are crucial for electrocatalytic CO$_2$ conversion to C$_{2+}$ products but face significant stability challenges. Structural reconstruction from Cu dissolution and reduction under negative potentials undermines their long-term stability. Herein, a novel Cu$_2$O@CeO$_x$ core-shell nanocatalyst is introduced, featuring a Cu$_2$O nanocube core encapsulated by an amorphous CeO$_x$ shell. Due to the facilitated electron transfer of abundant Cu/Ce interfaces, the CeO$_x$ shell layer simultaneously prevents the agglomeration and maintains the oxidation state of Cu$_2$O nanocubes, bringing in significantly improved stability. Unlike conventional coating layers, the defective CeO$_x$ shell uniquely avoids obstructing mass transfer while effectively promoting the activation of CO$_2$ and optimizing the electronic structure of Cu. The Cu$_2$O@CeO$_x$ nanocatalyst delivers a remarkable C$_{2+}$ Faradaic efficiency exceeding 80% at 300 mA cm^{-2} under a low applied potential of −0.98 V, with exceptional durability lasting over 50 h, compared to just 2 h for Cu$_2$O alone. This work presents an effective strategy to enhance catalyst stability without sacrificing activity, advancing the design of durable catalysts for electrocatalytic applications.

1. Introduction

Electrocatalytic carbon dioxide reduction reaction (CO$_2$RR) offers a sustainable approach to closing the carbon cycle by converting CO$_2$ into value-added products such as CO, HCOOH, CH$_4$, C$_2$H$_5$OH, C$_2$H$_4$, etc. Among these products, multi-carbon (C$_{2+}$) products, including C$_2$H$_4$, a vital chemical feedstock, and C$_2$H$_5$OH, a high-energy-density fuel, are particularly desirable.[1]

Y. Li, L. Sun, S. Liu, H. Li, Z. Song, J. Yu, L. Zhang
College of Chemistry and Environmental Engineering
Shenzhen University
Shenzhen 518060, P. R. China
E-mail: yujun@szu.edu.cn; lei.zhang@szu.edu.cn
J. Zou, Z. Guo
School of Chemical Engineering Faculty of Sciences
Engineering and Technology
The University of Adelaide
Adelaide, SA 5005, Australia
E-mail: zaiping.guo@adelaide.edu.au

A key step in producing C$_{2+}$ products is the C-C coupling process, which only takes place on Cu. Furthermore, the Cu$^+$ site is widely recognized for possessing lower energy for C-C coupling, in comparison to zero-valent or higher-valent Cu. Therefore, many researchers have focused on the optimization of Cu$^+$ sites in Cu-based catalysts for improving the faradaic efficiency of C$_{2+}$ products.[2]

Cu$_2$O nanoparticles with abundant Cu$^+$ sites have been widely used for C$_{2+}$ production.[3] Compared to polycrystalline Cu$_2$O, the Cu$_2$O nanocube exhibited superior C$_{2+}$ selectivity because of the enhanced C-C coupling reaction on their (100) facets.[3c] However, the stability of the Cu$_2$O nanocube is compromised by Cu$^+$ reduction at the negative potentials of CO$_2$RR and the dissolution of Cu ions, leading to aggregation and degradation of the reactive (100) facets.[3a,b] The instability of Cu$_2$O nanocubes, especially in flow-type devices, is a significant challenge. The C$_{2+}$/C$_{1+}$ product ratio drops dramatically from ≈3.5 to ≈1 accompanied by the current density declining from 300 to 150 mA cm^{-2} within 100 mins. Current modification strategies, such as creating heterointerfaces, help preserve the Cu$^+$ valence state in polycrystalline Cu$_2$O.[4] However, these methods are unable to maintain the crucial (100) facets of Cu$_2$O nanocubes. Moreover, both the Faradaic efficiency for C$_{2+}$ products and the stability (close to 60% for 25 h) must be significantly improved for industrial applications. This underscores the urgent need for strategies to stabilize Cu$_2$O nanocubes for higher C$_{2+}$ production.

Cerium dioxide (CeO$_2$) is widely recognized as an effective modifier in heterogeneous catalysis because of the reversible Ce^{4+}/Ce^{3+} redox transition.[5] The easy switch between Ce^{4+} and Ce^{3+} in CeO$_2$ has the potential to maintain the oxidation state of Cu. Additionally, the frustrated-Lewis pairs could be constructed in the defect-rich surface of CeO$_x$,[6] which promoted the adsorption and activation of CO$_2$ for CO$_2$ conversion.[7] Thus, using CeO$_x$ as the protection layer is promising to stabilize the inner Cu$_2$O nanocube without hindering CO$_2$ mass transfer or compromising activity. However, creating a thin, defective CeO$_x$ shell on the surface of the Cu$_2$O nanocube to optimize CO$_2$RR performance is challenging.

ADVANCED
SCIENCE NEWS
www.advancedsciencenews.com
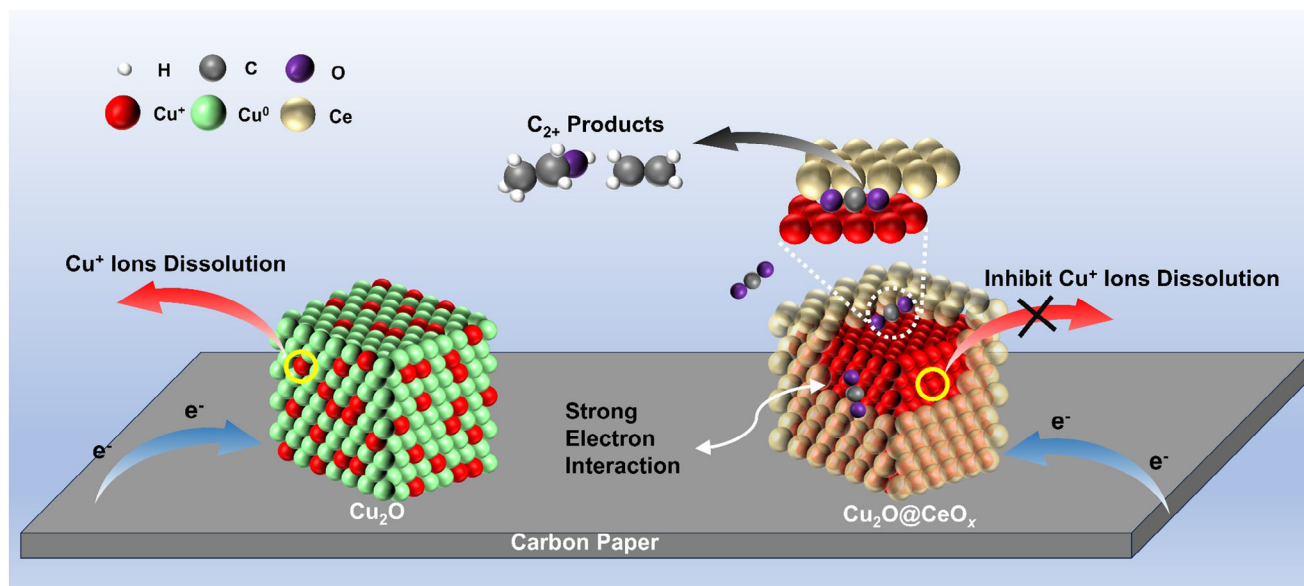
ADVANCED
FUNCTIONAL
MATERIALS
www.afm-journal.de

Figure 1. The design and advantages of $Cu_2O@CeO_x$ core–shell nanocatalyst supported on carbon paper for CO_2RR.

In this work, we successfully synthesized a core-shell structure of Cu_2O nanocube core covered with an amorphous CeO_x shell via a simple hydrothermal method by optimizing the adding ratio of Ce salt. As shown in **Figure 1**, the ultrathin CeO_x shell layer can inhibit the leaching of inside Cu ions and activate CO_2 for further reduction on the Cu_2O core. Meanwhile, the easy shift between Ce^{4+} and Ce^{3+} in CeO_x can facilitate the electron transfer and regulate the electronic structure of Cu for maintaining the oxidation state of Cu_2O in $Cu_2O@CeO_x$. Thus, the stability of $Cu_2O@CeO_x$ has been greatly improved while maintaining its high efficiency. The $Cu_2O@CeO_x$ catalyst delivers a high C_{2+} Faradaic efficiency (FE) of above 80% at 300 mA cm^{-2} under a low applied potential of −0.98 V, and the durability enhances from 2 h of Cu_2O to more than 50 h under the large current density of 300 mA cm^{-2} for $Cu_2O@CeO_x$.

2. Results and discussion

2.1. Synthesis and Structural Characterization of $Cu_2O@CeO_x$

The CuCe samples with varied Ce ratios were synthesized via a one-step hydrothermal process (details shown in the experimental part), and the morphology of CuCe3% is uniformly dispersed nanocubes (named as $Cu_2O@CeO_x$ in **Figure 2a**; Figure S1, Supporting Information). The high-resolution transmission electron microscope (HR-TEM) image of the nanocube is shown in Figure 2b. The lattice fringe of 0.21 nm corresponding to the (111) plane of Cu_2O was observed in the inner part, while no lattice fringes were detected in the thin surface layer (≈1.5 nm). The high-angle annular dark-field-scanning transmission electron microscopy (HAADF-STEM) image (Figure 2c; Figure S2a, Supporting Information) further confirms that the nanocube is covered with a thin semitransparent layer. The corresponding energy dispersive spectroscopy (EDS) mapping images (Figure 2c; Figure S2b, Supporting Information) show that only the signal of Ce and O were detected in the surface semitransparent layer,

and the signal of Cu was distributed uniformly in the inner part. These results indicate that the CuCe3% sample is a uniform nanocube structure with a crystal Cu_2O core covered with an amorphous CeO_x shell. So, the CuCe3% sample was named as $Cu_2O@CeO_x$. When increasing the adding content of Ce, the aggregated CeO_2 nanoparticles appeared beside the nanocube morphology in CuCe5% and CuCe8% (Figures S3, S4, Supporting Information). The reference sample of Cu_2O (Figure S5, Supporting Information) was synthesized using the same method with $Cu_2O@CeO_x$ without adding cerium salt.

The X-ray diffraction (XRD) patterns and the Raman spectroscopy of Cu_2O and $Cu_2O@CeO_x$ are shown in Figure 2d,e. Only the peaks ascribed to Cu_2O were observed in both Cu_2O and $Cu_2O@CeO_x$, further confirming the amorphous structure of CeO_x in $Cu_2O@CeO_x$. Also, nearly no angle shifts for Cu_2O diffraction peaks in $Cu_2O@CeO_x$ were detected compared with those of Cu_2O, consistent with the core-shell structure of $Cu_2O@CeO_x$ instead of Ce doping Cu_2O.[4b,5b] This finding is further corroborated by the extended X-ray absorption fine structure (EXAFS) spectra shown in Figure 2f. Similar to pure Cu_2O, only the Cu—O bond (≈1.5 Å) and Cu—O—Cu bond (≈3.1 Å) have existed in $Cu_2O@CeO_x$.[8]

XPS and X-ray absorption near edge structure (XANES) were employed to analyze the electronic structure of $Cu_2O@CeO_x$. The Cu $2p$ XPS spectrum (**Figure 3a**) shows that the peak of Cu $2p_{3/2}$ at 932.7 eV is attributed to Cu^0 or Cu^+.[9] The Cu LMM Auger spectrum (Figure S6, Supporting Information) further demonstrates the existence of Cu^+.[10] Significantly, the $Cu_2O@CeO_x$ exhibits an obvious shift in the Cu^0 or Cu^+ peak of the Cu $2p_{3/2}$ to the negative direction by 0.3 eV when compared with Cu_2O, suggesting the strong electronic interactions between Cu_2O and CeO_x.[5b,c] The XPS spectra of CuCe5% and CuCe8% (Figure S7, Supporting Information) reveal a consistent negative shift of 0.3 eV in the Cu $2p_{3/2}$ peak compared to pristine Cu_2O. This suggests that increasing the adding content of Ce does not induce additional electron transfer, and the
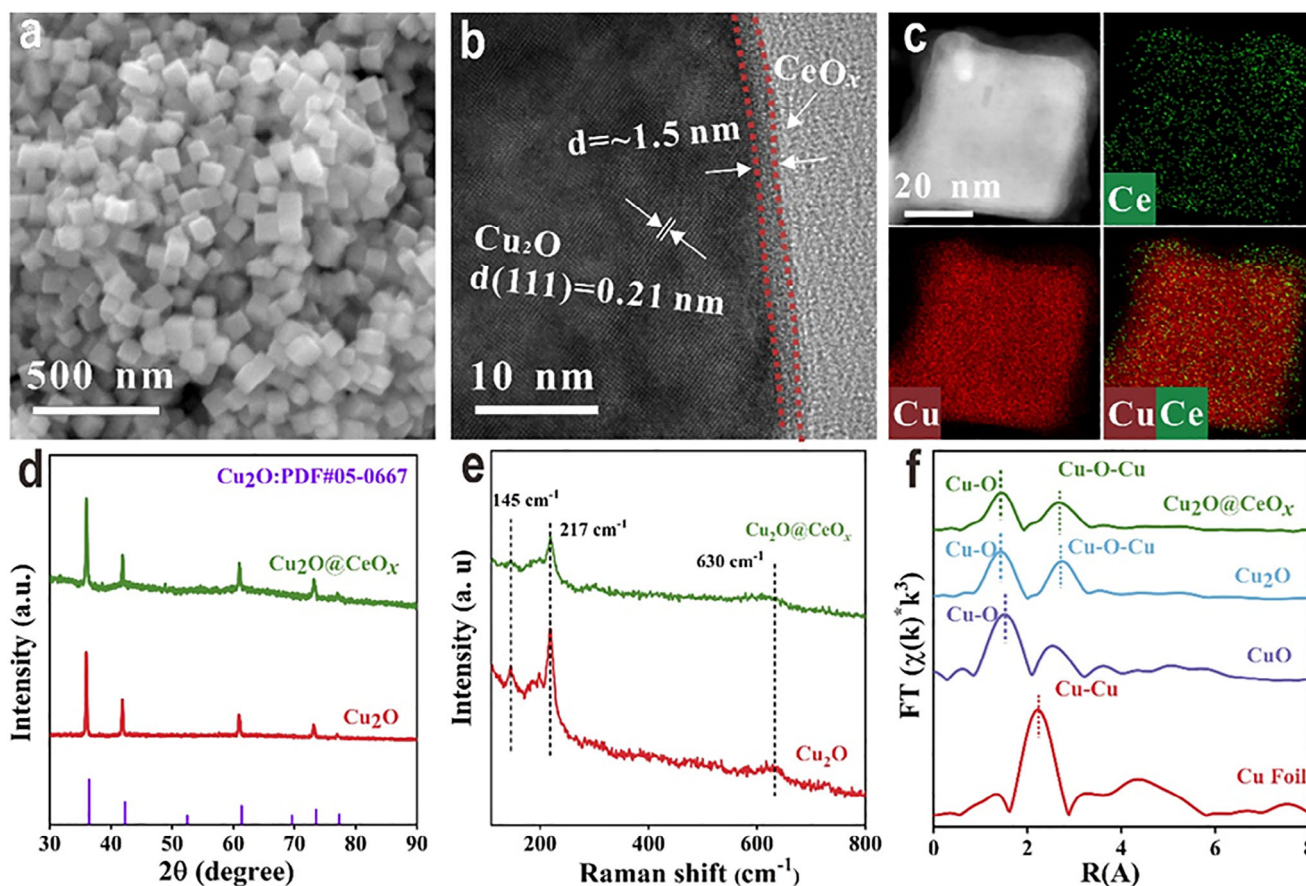
**ADVANCED
SCIENCE NEWS**

www.advancedsciencenews.com

**ADVANCED
FUNCTIONAL
MATERIALS**

www.afm-journal.de

Figure 2. Morphological and structural characterizations of $Cu_2O@CeO_x$. a) SEM image, b) HR-TEM image, and c) HAADF-STEM image and the corresponding EDS mapping images of $Cu_2O@CeO_x$. d) XRD patterns and e) Raman spectra of $Cu_2O@CeO_x$ and Cu_2O. f) Cu FT k^3-weighted EXAFS spectra of $Cu_2O@CeO_x$, CuO, Cu_2O, and Cu foil standards.

electron redistribution mainly occurs at the interface of CeO_x and Cu_2O. The XANES spectra (Figure 3b) also confirm this. The pre-edge line of $Cu_2O@CeO_x$ is between Cu foil and Cu_2O, indicating that the average valence state of Cu was between the metallic state and the cuprous state.[11] The Ce L_3-edge XANES spectrum (Figure 3c) shows that the Ce pre-edge line of $Cu_2O@CeO_x$ positions between $CeCl_3$ and CeO_2. The linear combination fitting (LCF) further shows that the ratio of Ce^{3+} is ≈48% (Figure S8 and Table S1, Supporting Information).[12] This is in excellent agreement with the ≈49% Ce^{3+} ratio determined from the Ce $3d$ XPS spectrum (Figure 3d), confirming the consistency and accuracy of our analysis. The much higher ratio of Ce^{3+} is from the amorphous structure of CeO_x and the electronic interactions between Cu_2O and CeO_x in $Cu_2O@CeO_x$.[5b,c,13] We then calculated the charge density difference of the optimized Ce_4O_7/Cu_2O model (Figures S9, S10, Supporting Information) to investigate the interfacial electronic effect between Cu_2O and CeO_x. As shown in Figure 3e, the charge is transferred from Ce_4O_7 to Cu_2O. Bader charge analysis further suggests that the overall Ce_4O_7 transfers 0.87 e^- to Cu_2O. The O $1s$ XPS spectra of $Cu_2O@CeO_x$ and Cu_2O are shown in Figure 3f. Compared with Cu_2O, a large number of oxygen vacancy defects are observed for $Cu_2O@CeO_x$, which result from its high ratio of Ce^{3+}. The abundant Ce^{3+} and oxygen vacancies of the CeO_x shell are beneficial for the activation of

CO_2,[7,14] and the Cu^+ sites from the Cu_2O core of $Cu_2O@CeO_x$ can promote C-C coupling to C_{2+} products.[2]

2.2. CO_2RR Performances and Reaction Mechanism

The electrochemical performances of Cu_2O and $Cu_2O@CeO_x$ toward the CO_2RR were evaluated in a flow cell with 1.0 м KOH solution as the electrolyte, and the carbon paper was used as the gas diffusion electrode (GDE). The polarization curves (without iR compensation) of Cu_2O and $Cu_2O@CeO_x$ were obtained in an Ar or CO_2 atmosphere (**Figure 4**a). The $Cu_2O@CeO_x$ catalyst exhibits a more positive onset potential and higher current densities in both environments, highlighting the positive contribution of the CeO_x layer to the overall electron transfer. Furthermore, in a CO_2 atmosphere, $Cu_2O@CeO_x$ achieves even higher current densities and a more positively shifted onset potential compared to Ar, demonstrating its efficiency for CO_2 reduction. To clarify the higher CO_2RR activity of $Cu_2O@CeO_x$, we conducted electrochemical impedance spectroscopy (EIS) measurements to assess the charge-transfer capacity of the catalysts.[15] As shown in Figure 4b, $Cu_2O@CeO_x$ has a smaller charge transfer resistance than Cu_2O. This indicates that the CeO_x with abundant Ce^{3+} and oxygen vacancies facilitates the electron transfer in $Cu_2O@CeO_x$.

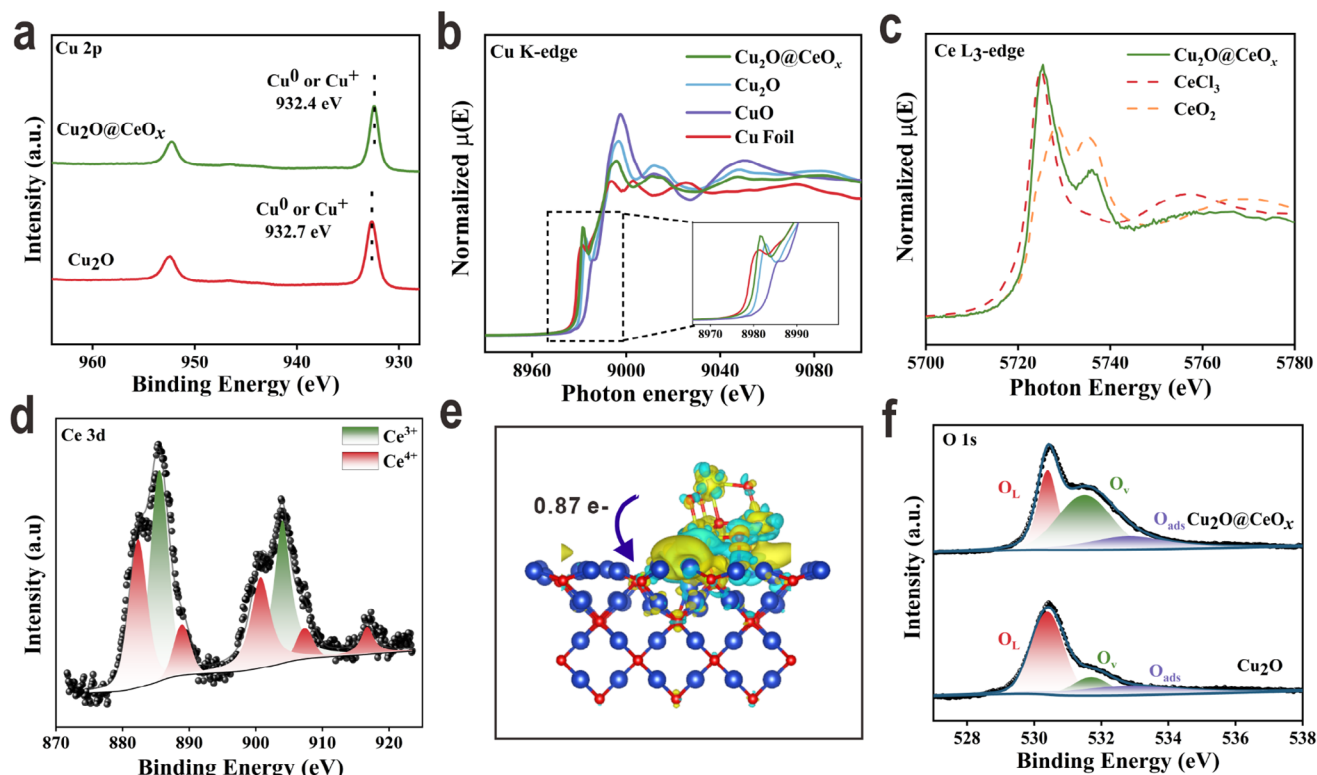**Figure 3.** Electronic interaction between Cu_2O and CeO_x. a) Cu 2p XPS spectra of $Cu_2O@CeO_x$ and Cu_2O. b) Cu K-edge XANES spectra of $Cu_2O@CeO_x$, CuO, Cu_2O, and Cu foil standards. c) Ce L_3-edge XANES spectra of $Cu_2O@CeO_x$, $CeCl_3$ and CeO_2 refer standards. d) Ce 3d XPS spectrum of $Cu_2O@CeO_x$. e) Differential charge density of Ce_4O_7/Cu_2O model (the cyan region reflects an electron-deficient state, whereas the yellow region reflects an electron-rich area). f) O 1s XPS spectra of $Cu_2O@CeO_x$ and Cu_2O.

Then we discuss the effect of the CeO_x shell on the selectivity of CO_2RR products. We utilized a 30-min constant current method for testing purposes. Gas chromatography effectively detected the resulting gas phase products (Figure S11, Supporting Information), and nuclear magnetic resonance (NMR) spectroscopy was employed to detect the liquid phase products (Figure S12, Supporting Information). As shown in Figure 4c and Figure S13 (Supporting Information), the CO_2RR products for Cu_2O and $Cu_2O@CeO_x$ are nearly the same. The CO_2RR products are dependent on current density due to the increasing applied potentials.[11] The FE of the C_{2+} products of $Cu_2O@CeO_x$ (Figure 4d) is higher than that of Cu_2O starting from the large current density of 200 mA cm^{-2}. $Cu_2O@CeO_x$ exhibits the highest FE of 81.8% at a current of 300 mA cm^{-2}. Moreover, the applied potentials of $Cu_2O@CeO_x$ (Figure 4d) are much lower to reach the same current densities than those of Cu_2O. This indicates that the ultrathin CeO_x shell does not hinder the mass transfer of CO_2RR, but rather has the potential to enhance the adsorption and activation of CO_2 (discussed below). For CuCe5% and CuCe8%, the presence of a thicker CeO_x shell leads to the declined FE of C_{2+} products as shown in Figure S14 (Supporting Information). Notably, the CuCe8% sample exhibits a marked reduction in FE for C_{2+} products to 50.6% at 300 mA cm^{-2}, accompanied by an increase in the FE of CH_4. This selectivity shift may originate from the enhanced hydrogenation capacity of the thicker CeO_2 nanoparticle shell, which disrupts the C-C coupling pathway while promoting the sequential hydrogenation of $^*CO$

intermediates toward the formation of methane.[14] The long-term stability performance of $Cu_2O@CeO_x$ is shown in Figure 4f. The potential remains steady and the FE of C_{2+} products maintains above 80% under the large current density of 300 mA cm^{-2} for 50 h, demonstrating the excellent stability of $Cu_2O@CeO_x$. The high C_{2+} FE and long durability time under the large current density of 300 mA cm^{-2} make $Cu_2O@CeO_x$ comparable with those of the state-of-the-art CO_2RR electrocatalysts (Figure 4e).

To further elucidate the key intermediates and gain a deeper understanding of the CO_2RR mechanism, we collected in situ surface enhanced Raman scattering (SERS, Figure S15, Supporting Information) spectra and in situ attenuated total reflectance surface enhanced infrared absorption spectroscopy (ATR-SEIRAS). As shown in **Figure 5a**, the peak at 373 cm^{-1} is attributed to the Cu—CO stretching,[16] which represents a strong interaction between Cu and $^*CO$.[17] This indicates that CO_2RR occurs on the surface of the Cu_2O inner core, and the CeO_x shell does not inhibit the mass transfer for the reaction. As the potential becomes more negative, the peak at 529 cm^{-1} ascribed to $^*CH_2CHO$ becomes obvious while the peak at 1064 cm^{-1} ascribed to carbonate decreases remarkably.[18] This indicates the CO_2RR progresses vigorously for the generation of C_{2+} products over $Cu_2O@CeO_x$. In situ ATR-SEIRAS spectroscopy (Figure 5b) further detects peaks around 1245, 1190 and 1589 cm^{-1} corresponding to $^*CHO$, the C≡O stretching band of $^*COCHO$ and symmetric $^*COCHO$, respectively.[19] The $^*OCCHO$ is the key intermediate revealing the pathway of C-C coupling between $^*CO$

**ADVANCED
SCIENCE NEWS**
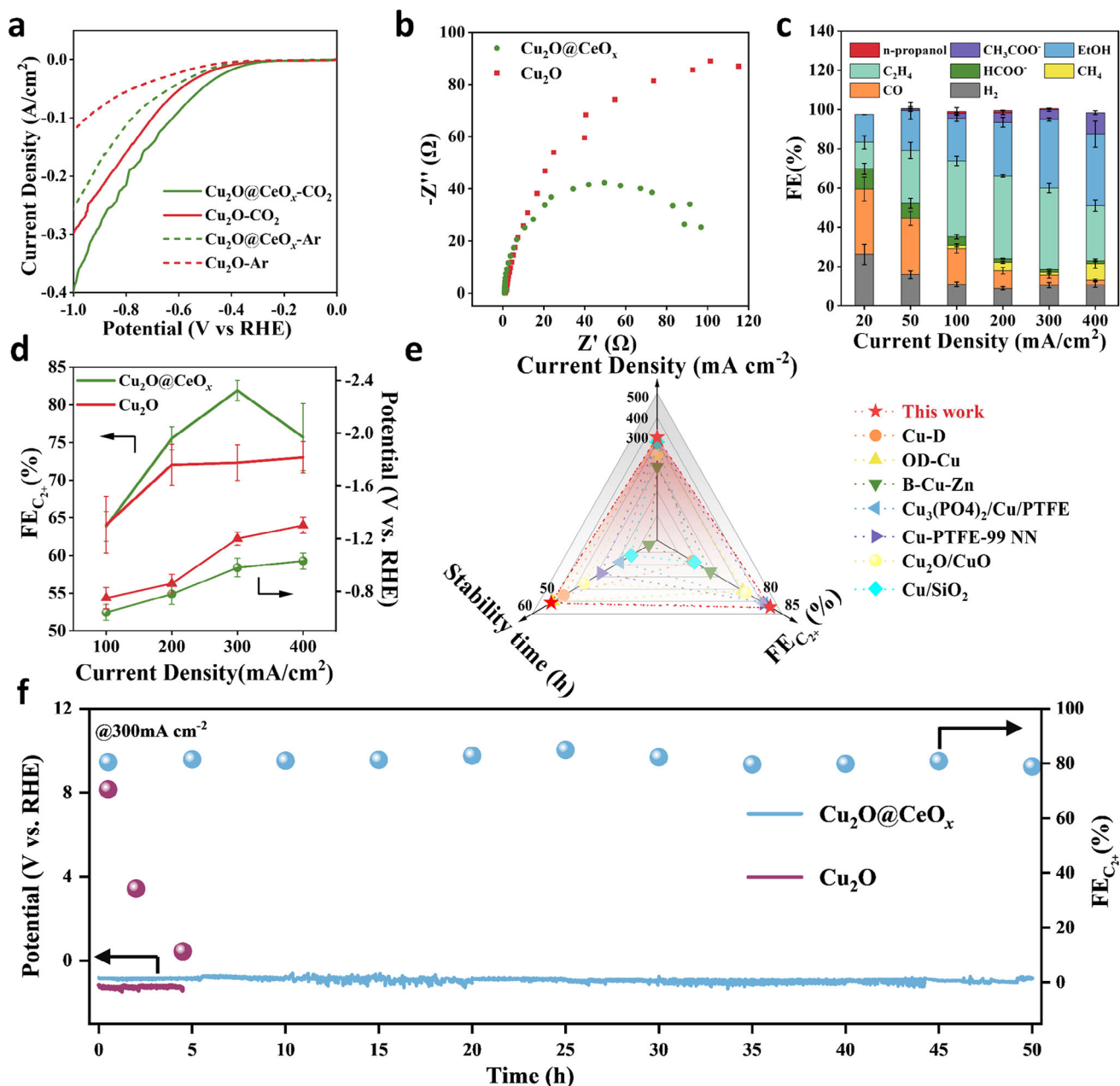
www.advancedsciencenews.com

**ADVANCED
FUNCTIONAL
MATERIALS**

www.afm-journal.de

Figure 4. Electrochemical CO_2RR performances. a) LSV curves in different atmospheres and b) Nyquist plots of Cu_2O and $Cu_2O@CeO_x$. c) The measured FEs of $Cu_2O@CeO_x$ under different current densities. d) The C_{2+} FEs (left Y-axis) and potentials (right Y-axis) of Cu_2O and $Cu_2O@CeO_x$ under different current densities. e) Comparisons of FE of C_{2+}, the current density, and stability test time over $Cu_2O@CeO_x$ and typical Cu-based catalysts reported. Detailed data are shown in Table S2, Supporting Information. f) Time-dependent potentials (left Y-axis) and C_{2+} FEs (right Y-axis) for $Cu_2O@CeO_x$ and Cu_2O recorded at 300mA cm^{-2}.

and *CHO.[20] The intensity of *CHO for $Cu_2O@CeO_x$ is obviously higher than that of Cu_2O (Figure S16, Supporting Information), indicating the greater hydrogenation capacity due to the water-splitting ability of CeO_x as reported previously.[8b,21] Peaks at 1165 and 1310 cm^{-1} attributed to the *OC_2H_5 are also observed for $Cu_2O@CeO_x$, which are generally considered to be the crucial intermediate for ethanol.[22]

As shown in Figure 5c, the peak at 2350 cm^{-1} attribute to the activated *CO_2 is more pronounced over $Cu_2O@CeO_x$

than over Cu_2O, indicating the better ability of $Cu_2O@CeO_x$ for the activation of CO_2. The DFT calculations in Figure 5d show that the adsorption energy for CO_2 adsorption is markedly lower over CeO_x than over Cu_2O (Figures S17–S19, Supporting Information). This further demonstrates the CeO_x shell in $Cu_2O@CeO_x$ can promote the activation and adsorption of CO_2. The free energy diagrams from *CO_2 to *OCCHO over Cu sites of the optimized $Cu_2O(100)$ model (Figure S20, Supporting Information) and $Ce_4O_7/Cu_2O(100)$ model (Figure S9, Supporting

**ADVANCED
SCIENCE NEWS**

www.advancedsciencenews.com

**ADVANCED
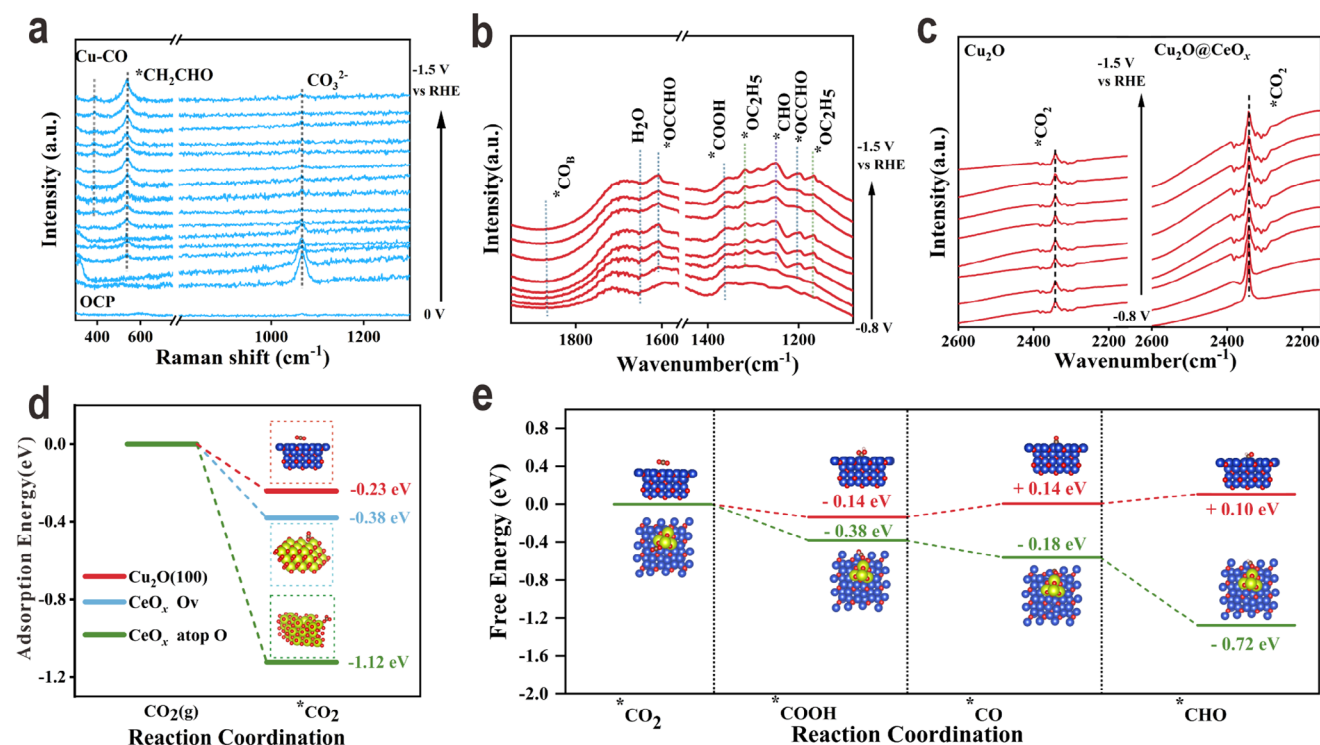FUNCTIONAL
MATERIALS**

www.afm-journal.de

Figure 5. CO_2RR mechanism investigation. In situ a) SERS spectra collected at different potentials over $Cu_2O@CeO_x$ and b) ATR-SEIRAS spectra. c) The peak for the adsorption of CO_2 from the in situ ATR-SEIRAS spectra of $Cu_2O@CeO_x$ and Cu_2O. Calculated d) adsorption energy for the $^*CO_2$ adsorption and e) free energy diagrams from $^*CO_2$ to $^*OCCHO$ over Cu sites and the corresponding models of CO_2RR on $Cu_2O(100)$ (Red line) and $Ce_4O_7/Cu_2O(100)$ (Green line). The yellow, blue, grey, red, and white balls represent Ce, Cu, C, O, and H, respectively.

Information) are also compared as shown in Figure 5e and Figure S21 (Supporting Information). The corresponding DFT models are shown in Figures S22 and S23 (Supporting Information). The formation energy of the key $^*CHO$ intermediate is much lower over $Ce_4O_7/Cu_2O(100)$ than over Cu_2O, consistent with the in situ ATR-SEIRAS results. The easier formation of $^*CHO$ can promote the next C-C coupling step for C_{2+} products (Figure S21, Supporting Information). Thus, the CeO_x shell can not only promote the activation of CO_2 but also benefit the Cu_2O core the hydrogen step for the key $^*CHO$ intermediate of C-C coupling.

2.3. Discussion on the High Stability of $Cu_2O@CeO_x$

In this section, we will discuss the exceptional stability of $Cu_2O@CeO_x$. The 4.5-h constant CO_2RR tests at 300 mA cm^{-2} was performed for Cu_2O (**Figure 6a**) and $Cu_2O@CeO_x$ (Figure 6b). For Cu_2O, The FE of C_2H_4 decreases drastically starting from 2 h along with the increase of the FE of H_2. In the end, the FE of C_2H_4 decreases to below 10% and the FE of H_2 reaches above 70%. In contrast, the FEs of C_2H_4 and H_2 only fluctuate slightly within the 4.5 h for $Cu_2O@CeO_x$ (Figure 6b). These results demonstrate the positive effect of the CeO_x shell on the stability of Cu_2O for CO_2RR.

To further investigate the mechanism of stability enhancement in $Cu_2O@CeO_x$, the morphologies of Cu_2O and $Cu_2O@CeO_x$ after stability tests were obtained first. The uniform distributed nanoparticles in fresh Cu_2O (Figure S24, Supporting Informa-

tion) aggregate and form the porous honeycomb structure for Cu_2O-4.5h (Figure 6c), indicating a significant structural reconstruction has occurred for Cu_2O during the constant CO_2RR. For $Cu_2O@CeO_x$-4.5h (Figure 6d), the morphology of the uniformly distributed nanoparticles is still present. This significant difference demonstrates that the CeO_x shell layer can prevent Cu_2O from dissolution (Figure S25, Supporting Information) and reconstruction. To obtain the chemical state of Cu after the stability tests, we collected both XRD (Figure 6e) and Cu LMM (Figure 6f) patterns. The XRD pattern shows that the peaks of Cu at 43° and 50° corresponding to the (111) and (200) planes of metal Cu appear in Cu_2O-4.5h. Moreover, the intensity of the Cu(111) peak at 43° is basically the same as the peak of $Cu_2O(111)$ at 36°, indicating that a large number of Cu ions are reduced to metal Cu for Cu_2O-4.5h. While for $Cu_2O@CeO_x$-4.5h, the intensity of the Cu(111) peak is very low and the peak of Cu(200) can hardly be seen, illustrating most of Cu in $Cu_2O@CeO_x$ remains oxidation state. Also, the Cu LMM Auger spectra exhibit that the peak of Cu^+ in Cu_2O (Figure 6e) is significantly shifted toward Cu^0 (918.6 eV) in Cu_2O-4.5h, while $Cu_2O@CeO_x$-4.5h remains in Cu^+ (916.7 eV). To verify the protective effect of the CeO_x shell on the valence state more intuitively, we compared the CV curves under the Ar atmosphere (Figure S26, Supporting Information), and the copper redox of $Cu_2O@CeO_x$ is obviously inhibited.

To make a short summary, the CeO_x shell, on one hand, can prohibit the Cu_2O nanoparticle core from aggregation and structural reconstruction by stable Cu ions from leaching and
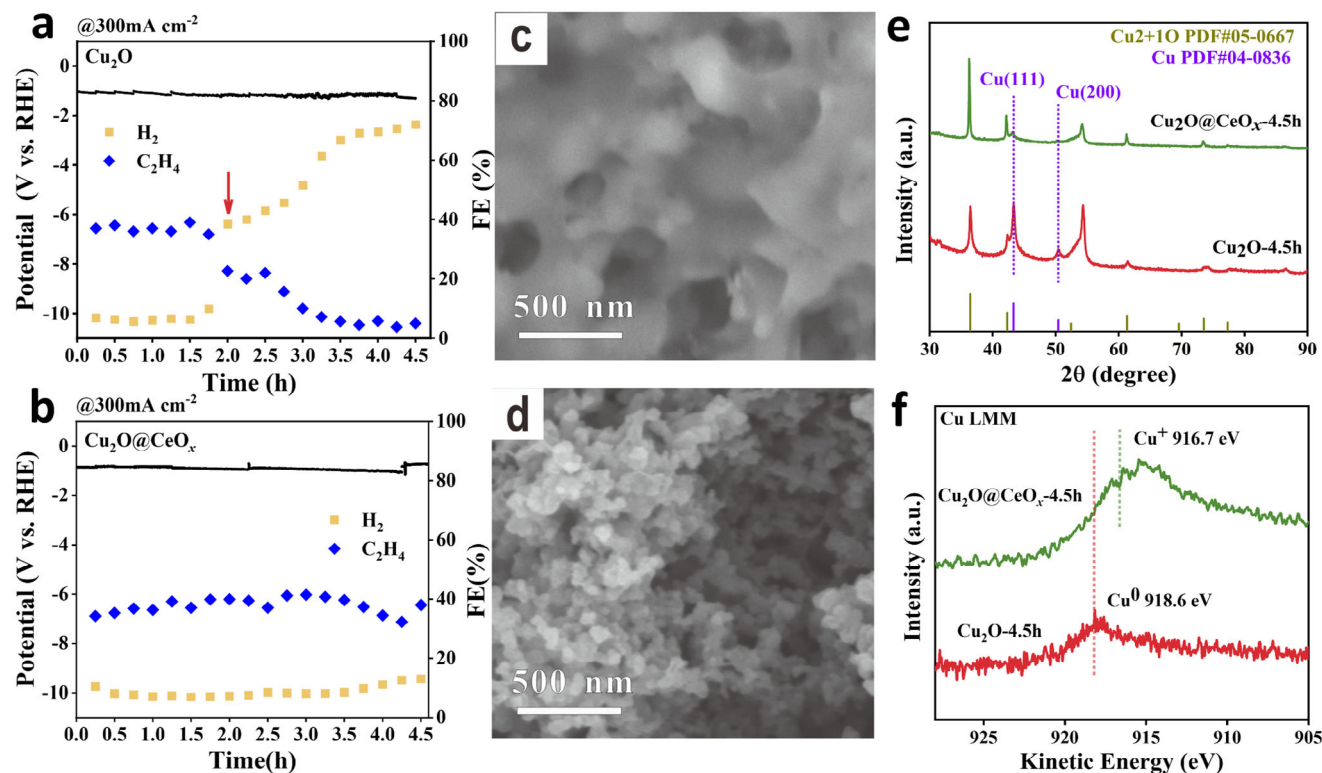
**ADVANCED
SCIENCE NEWS**

www.advancedsciencenews.com

**ADVANCED
FUNCTIONAL
MATERIALS**

www.afm-journal.de

Figure 6. Stability improvement investigation. 4.5-h constant CO_2RR tests at 300 mA cm^{-2} for a) Cu_2O and b) $Cu_2O@CeO_x$. SEM images after 4.5 h tests of c) Cu_2O and d) $Cu_2O@CeO_x$. e) Cu LMM Auger spectra and f) XRD patterns of $Cu_2O@CeO_x$ and Cu_2O after 4.5 h tests.

dissolution. On another hand, the CeO_x shell can maintain the oxidation state of Cu due to the facilitated electron transfer and the easy shift between Ce^{4+} and Ce^{3+}.[5a,23]

3. Conclusion

In summary, we developed a highly efficient and stable core-shell structure electrocatalyst composed of Cu_2O nanocube core and CeO_x shell for CO_2RR. In situ, spectroscopy and DFT calculations demonstrate that the CeO_x shell promotes the activation of CO_2 and optimizes the electronic structure of the Cu_2O core for the decreasing energy barrier of $^*CHO$, which is the key intermediate for C-C coupling. The $Cu_2O@CeO_x$ catalyst shows an enhanced C_2 FE of 81.8% and a decreased applied potential of −0.98 V at 300 mA cm^{-2} compared with 72% and −1.2 V of Cu_2O. More importantly, $Cu_2O@CeO_x$ delivers long-term stability of 50 h under the larger current density of 300 mA cm^{-2}, while the Cu_2O catalyst only lasts 2 h. The greatly improved stability of $Cu_2O@CeO_x$ resulted from the CeO_x shell that maintains the morphology and valence state of the Cu_2O core. This work paves the way for improving the activity and stability of unstable metal electrocatalysts at the same time toward various energy applications.

Supporting Information

Supporting Information is available from the Wiley Online Library or from the author.

Conflict of Interest

The authors declare no conflict of interest.

Data Availability Statement

The data that support the findings of this study are available from the corresponding author upon reasonable request.

[1] a) W. Lai, Y. Qiao, J. Zhang, Z. Lin, H. Huang, *Energy Environ. Sci.* **2022**, *15*, 3603; b) E. W. Lees, B. A. W. Mowbray, F. G. L. Parlane, C. P. Berlinguette, *Nat. Rev. Mater.* **2021**, *7*, 55; c) M. L. Yu, P. F. Sui, X. Z. Fu, J. L. Luo, S. B. Liu, *Adv. Energy Mater.* **2023**, *13*, 2203191.

[2] a) S. Li, J. Yu, S. Zhang, W. Qiu, X. Tang, Z. Lin, R. Cai, Y. Fang, S. Yang, X. Cai, *Adv. Funct. Mater.* **2023**, *34*, 2311989; b) L. Ding, N. Zhu, Y. Hu, Z. Chen, P. Song, T. Sheng, Z. Wu, Y. Xiong, *Angew. Chem., Int. Ed.* **2022**, *61*, 61; c) J. Feng, L. Wu, S. Liu, L. Xu, X. Song, L. Zhang, Q. Zhu, X. Kang, X. Sun, B. Han, *J. Am. Chem. Soc.* **2023**, *145*, 9857; d) P. P. Albertini, M. A. Newton, M. Wang, O. Segura Lecina, P. B. Green, D. C. Stoian, E. Oveisi, A. Loiudice, R. Buonsanti, *Nat. Mater.* **2024**, *23*, 680.

[3] a) S. Popović, M. Smiljanić, P. Jovanovič, J. Vavra, R. Buonsanti, N. Hodnik, *Angew. Chem., Int. Ed.* **2020**, *59*, 14736; b) Q. Lei, H. Zhu, K. Song, N. Wei, L. Liu, D. Zhang, J. Yin, X. Dong, K. Yao, N. Wang, X. Li, B. Davaasuren, J. Wang, Y. Han, *J. Am. Chem. Soc.* **2020**, *142*, 4213; c) P. Grosse, D. Gao, F. Scholten, I. Sinev, H. Mistry, B. Roldan Cuenya, *Angew. Chem., Int. Ed.* **2018**, *57*, 6192; d) W. Choi, Y. Chae, E. Liu, D. Kim, W. S. Drisdell, H.-s. Oh, J. H. Koh, D. K. Lee, U. Lee, D. H. Won, *Nat. Commun.* **2024**, *15*, 8345.

[4] a) X. Liu, T. Liu, T. Ouyang, J. Deng, Z.-Q. Liu, *Angew. Chem., Int. Ed.* **2024**, *64*, 202419796; b) Y. Sun, J. Xie, Z. Fu, H. Zhang, Y. Yao, Y. Zhou, X. Wang, S. Wang, X. Gao, Z. Tang, S. Li, X. Wang, K. Nie, Z. Yang, Y.-M. Yan, *ACS Nano* **2023**, *17*, 13974.

[5] a) X. Zhou, J. Shan, L. Chen, B. Y. Xia, T. Ling, J. Duan, Y. Jiao, Y. Zheng, S.-Z. Qiao, *J. Am. Chem. Soc.* **2022**, *144*, 2079; b) J. Yu, J. Wang, X. Long, L. Chen, Q. Cao, J. Wang, C. Qiu, J. Lim, S. Yang, *Adv. Energy Mater.* **2021**, *11*, 2002731; c) H. Liu, J. Yu, J. Lin, B. Feng, M. Sun, C. Qiu, K. Qian, Z. Si, B. Huang, J.-J. Delaunay, Y. Ikuhara, S. Yang, *EES Catal.* **2023**, *1*, 720; d) S. Das, R. Bhaskar, K. B. Narayanan, *J. Rare Earths* **2024**, *42*, 1817.

[6] S. Zhang, Z.-Q. Huang, Y. Ma, W. Gao, J. Li, F. Cao, L. Li, C.-R. Chang, Y. Qu, *Nat. Commun.* **2017**, *8*, 15266.

[7] S. Zhang, Z. Xia, Y. Zou, F. Cao, Y. Liu, Y. Ma, Y. Qu, *J. Am. Chem. Soc.* **2019**, *141*, 11353.

[8] a) W.-F. Xiong, D.-H. Si, H.-F. Li, X. Song, T. Wang, Y.-B. Huang, T.-F. Liu, T. Zhang, R. Cao, *J. Am. Chem. Soc.* **2023**, *146*, 289; b) S. Li, G. Wu, J. Mao, A. Chen, X. Liu, J. Zeng, Y. Wei, J. Wang, H. Zhu, J. Xia,

X. Wang, G. Li, Y. Song, X. Dong, W. Wei, W. Chen, *Angew. Chem., Int. Ed.* **2024**, *63*, 202407612.

[9] a) L. Sun, Z. Song, M. Lin, J. Peng, Y. Li, R. Wei, Q. Zhang, J. Yu, L. Zhang, *ACS Sustainable Chem. Eng.* **2024**, *12*, 9748; b) S. Li, H. Duan, J. Yu, C. Qiu, R. Yu, Y. Chen, Y. Fang, X. Cai, S. Yang, *ACS Catal.* **2022**, *12*, 9074.

[10] T. T. Zhao, J. H. Li, J. D. Liu, F. M. Liu, K. Q. Xu, M. Yu, W. C. Xu, F. Y. Cheng, *ACS Catal.* **2023**, *13*, 4444.

[11] X. K. Lu, B. Lu, H. Li, K. Lim, L. C. Seitz, *ACS Catal.* **2022**, *12*, 6663.

[12] B. Ravel, M. Newville, *J. Synchrotron Radiat.* **2005**, *12*, 537.

[13] H. Liu, H. Duan, J. Yu, C. Qiu, R. Yu, J. Gao, S. Li, X. Du, Z. Si, S. Yang, *ACS Mater. Lett.* **2022**, *4*, 2572.

[14] R. Yu, C. Qiu, Z. Lin, H. Liu, J. Gao, S. Li, Y. Yao, J. Yu, S. Yang, *ACS Mater. Lett.* **2022**, *4*, 1749.

[15] F. Dong, H. Duan, Z. Lin, H. Yuan, M. Ju, X. Du, J. Gao, J. Yu, S. Yang, *Appl. Catal. B-Environ.* **2024**, *340*, 123242.

[16] a) R. Amirbeigiarab, J. Tian, A. Herzog, C. Qiu, A. Bergmann, B. Roldan Cuenya, O. M. Magnussen, *Nat. Catal.* **2023**, *6*, 837; b) Y. Cao, Z. Chen, P. Li, A. Ozden, P. Ou, W. Ni, J. Abed, E. Shirzadi, J. Zhang, D. Sinton, J. Ge, E. H. Sargent, *Nat. Commun.* **2023**, *14*, 2387.

[17] J. Jiao, X. Kang, J. Yang, S. Jia, Y. Peng, S. Liu, C. Chen, X. Xing, M. He, H. Wu, B. Han, *J. Am. Chem. Soc.* **2024**, *146*, 15917.

[18] a) Y. Zhao, X.-G. Zhang, N. Bodappa, W.-M. Yang, Q. Liang, P. M. Radjenovica, Y.-H. Wang, Y.-J. Zhang, J.-C. Dong, Z.-Q. Tian, J.-F. Li, *Energy Environ. Sci.* **2022**, *15*, 3968; b) X. Lu, C. Zhu, Z. Wu, J. Xuan, J. S. Francisco, H. Wang, *J. Am. Chem. Soc.* **2020**, *142*, 15438.

[19] P. Wang, H. Yang, C. Tang, Y. Wu, Y. Zheng, T. Cheng, K. Davey, X. Huang, S.-Z. Qiao, *Nat. Commun.* **2022**, *13*, 3754

[20] a) W. Zhang, C. Huang, Q. Xiao, L. Yu, L. Shuai, P. An, J. Zhang, M. Qiu, Z. Ren, Y. Yu, *J. Am. Chem. Soc.* **2020**, *142*, 11417; b) S. Zhu, T. Li, W.-B. Cai, M. Shao, *ACS Energy Lett.* **2019**, *4*, 682.

[21] C. Xia, X. Wang, C. He, R. Qi, D. Zhu, R. Lu, F.-M. Li, Y. Chen, S. Chen, B. You, T. Yao, W. Guo, F. Song, Z. Wang, B. Y. Xia, *J. Am. Chem. Soc.* **2024**, *146*, 20530.

[22] a) X. Li, S. Wang, L. Li, Y. Sun, Y. Xie, *J. Am. Chem. Soc.* **2020**, *142*, 9567; b) F. Xu, B. Feng, Z. Shen, Y. Chen, L. Jiao, Y. Zhang, J. Tian, J. Zhang, X. Wang, L. Yang, Q. Wu, Z. Hu, *J. Am. Chem. Soc.* **2024**, *146*, 9365.

[23] a) Z. Dong, C. Zhou, W. Chen, F. Lin, H. Luo, Z. Sun, Q. Huang, R. Zeng, Y. Tan, Z. Xiao, H. Huang, K. Wang, M. Luo, F. Lv, S. Guo, *Adv. Funct. Mater.* **2024**, *34*, 2400809; b) D. Pang, W. Li, N. Zhang, H. He, S. Mao, Y. Chen, L. Cao, C. Li, A. Li, X. Han, *J. Rare Earth* **2024**, *42*, 676. c) H. Liu, Q. Zhou, J. Yu, M. Nakabayashi, Y.-T. Lee, N. Shibata, Y. Li, J.-J. Delaunay, *ACS Catal.* **2025**, *15*, 8511.